ACS APPLIED MATERIALS & INTERFACES

Research Article

www.acsami.org

Controlled Film Architectures to Detect a Biomarker for Pancreatic Cancer Using Impedance Spectroscopy

Andrey C. Soares,*[,†,‡] Juliana C. Soares,[†] Flavio M. Shimizu,[†] Matias E. Melendez,[§] André L. Carvalho,[§] and Osvaldo N. Oliveira, Jr.[†]

[†]São Carlos Institute of Physics, University of São Paulo, 13560-970 São Carlos, São Paulo Brazil

[‡]São Carlos School of Engineering, University of São Paulo, 13560-000 São Carlos, São Paulo, Brazil

[§]Barretos Cancer Hospital, 14784-400 Barretos, São Paulo, Brazil

Supporting Information

ABSTRACT: The need for analytical devices for detecting cancer at early stages has motivated research into nanomaterials where synergy is sought to achieve high sensitivity and selectivity in low-cost biosensors. In this study, we developed a film architecture combining self-assembled monolayer (SAM) and layer-by-layer (LbL) films of polysaccharide chitosan and the protein concanavalin A, on which a layer of anti-CA19−9 antibody was adsorbed. Using impedance spectroscopy with this biosensor, we were capable of detecting low concentrations of the antigen CA19−9, an important biomarker for pancreatic cancer. The limit of detection of 0.69U/mL reached is sufficient for detecting pancreatic cancer at very early stages. The selectivity of the biosensor was inferred from a series of control experiments with samples of cell lines that were tested positive (HT29) and negative (SW620) for the biomarker CA19−9, in addition to the lack of changes in the capacitance value for other analytes and antigen that are not related to this type of cancer. The high sensitivity and selectivity are ascribed to the very specific antigen−antibody interaction, which was confirmed with PM-IRRAS and atomic force microscopy. Also significant is that used information visualization methods to show that different cell lines and commercial samples containing distinct concentrations of CA19−9 and other analytes can be easily distinguished from each other. These computational methods are generic and may be used in optimization procedures to tailor biosensors for specific purposes, as we demonstrated here by comparing the performance of two film architectures in which the concentration of chitosan was varied.

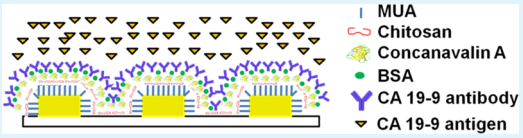

KEYWORDS: *pancreatic cancer, biosensors, nanostructured films, CA19−9, impedance spectroscopy, information visualization*

INTRODUCTION

The development of methodologies for the early diagnostics of cancer appears to be an inevitable trend owing to the improved therapy efficacy and even prevention of relapse by the patient.[1] One possible way to reach such an ambitious target is to identify biomarkers associated with the different types of cancer,[1,2] which can be detected with analytical devices at early stages of the disease or even before. There is ample demonstration in the literature that analytical sciences are sufficiently mature for detecting biomarkers with high sensitivity and selectivity,[3−5] in many cases relying on nanotechnology. The importance of nanomaterials and nanostructured films, for instance, has been highlighted[6] with particular emphasis on the synergy achieved upon combining distinct types of materials in the sensing units. Moreover, a variety of experimental methods are now available for the detection.

The main challenges remaining for reaching early diagnosis and even prognosis are related to the identification of very specific biomarkers, and to the need of producing sensors and biosensors satisfying the stringent requirements for real-world application in clinical analysis. Diagnosis and prognosis biomarkers play important roles in individualizing treatment decisions. In this way, early detection of pancreatic cancer may allow an improved patient prognosis, making possible a surgery treatment with curative intent. More specifically, these devices must be sufficiently robust and relatively low cost. Several groups have therefore focused on immunosensors working with optical and electrical measurements as the principles of detection[6−9] in which the sensing units are made with nanostructured films, including self-assembled monolayers (SAMs)[10,11] and layer-by-layer (LbL) films.[12,13] These film-fabrication methods have been proven suitable for immunosensors (and biosensors in general) because of their preserving the activity of immobilized biomolecules. Furthermore, whereas the choice of materials is rather limited for SAMs, many are the materials that can be combined in the form of LbL films.

In this study, we exploit the control of molecular architectures provided by SAMs and LbL technologies to produce immunosensors for detecting a biomarker associated with pancreas cancer. The biomarker is the sialylated Lewis carbohydrate antigen 19−9 (CA19−9),[14,15] a high-molecular-

Received: September 14, 2015
Accepted: November 5, 2015
Published: November 5, 2015

DOI: 10.1021/acsami.5b08666
ACS Appl. Mater. Interfaces 2015, 7, 25930−25937

weight mucin protein generally used to detect the presence of cancer through its levels in blood serum.[16−18] CA19−9 serum levels may be elevated in patients with nonmalignant diseases or other gastrointestinal cancers as well,[19] but a recent meta-analysis observed that CA19−9 serum levels showed better performance in the diagnosis of pancreatic cancer than other biomarkers.[20] Moreover, the prognostic value of peri-operative CA 19−9 levels and its role as an indicator of asymptomatic recurrence have been investigated in patients with resectable pancreatic cancer,[21,22] and a recent phase III trial confirmed the prognostic value of postresection CA 19−9 levels in patients undergoing surgery with curative intent.[23] In spite of its change in specificity according to the patient symptoms,[24] CA19−9 is the only biomarker approved by the U.S Food and Drug Administration for pancreas cancer.[25]

The immunosensors are built by immobilizing anti-CA19−9 antibodies on a matrix made with a SAM monolayer coated by one layer of chitosan, a biocompatible polysaccharide, and one layer of concanavalin A (Con A). The film architecture was selected to warrant available sites of the antibodies for adsorption of CA19−9 molecules, which then altered the film properties considerably. We detected such changes using impedance spectroscopy and reached high sensitivity and selectivity, thus allowing to detect CA19−9 in cell lines, in addition to commercial samples with the biomarker added to a buffer. This high performance is also attributed to the use of information visualization methods to treat the data.[26−28] We also determined the mechanism behind the detection with polarization-modulated infrared reflection absorption spectroscopy (PM-IRRAS) and atomic force microscopy. A comparison is also made with the performance of other immunosensors to detect CA19−9 from the literature.[4,5]

EXPERIMENTAL SECTION

Electrode Modification. Detection was performed with the biosensor (immunosensor) architecture depicted in Figure 1, featuring gold electrodes coated with a self-assembled monolayer (SAM), on which a bilayer of chitosan and concanavalin A (Con A) was adsorbed. Then a layer of anti-CA19−9 antibodies was deposited. The buildup of the biosensor was as follows. Gold interdigitated electrodes with 3 mm^2, containing 50 pairs of fingers (10 μm width and spaced by 10 μm) were fabricated onto Bk7 glass substrates by optical lithography and lift-off. Before use the electrodes were cleaned with UV/ozone following the procedure of Ron and collaborators,[29] and then coated with a SAM of 11-mercaptoundecanoic acid (11-MUA) (Sigma-Aldrich, USA) adsorbed from a 1 mM solution during 48h. These electrodes should exhibit negatively charged COO^- groups, which are useful for adsorbing in the next step a layer of chitosan (Galena, Brazil,) from aqueous solutions of distinct concentrations (0.3, 0.5, 1.0, and 2.0 mg/mL) during 2 h. The modified electrode was then coated with a layer of Con A (Sigma-Aldrich, USA) from a 1 mg/mL aqueous solution during 2 h. In order to prepare for adsorption of antibodies, the carboxylated groups of Con A amino acids were activated by incubation in 0.1 M N-Hydroxisuccinimide (NHS) (Sigma-Aldrich, USA) /0.1 M 1-Ethyl-3-(3-dimethyllaminopropyl) carbodiimide (EDC) (Sigma-Aldrich, USA) for 24h. The final layer of the biosensor contained anti-CA19−9 antibodies (Aviva System Biology, USA), adsorbed during 45 min and washed with deionized water. After antibody modification, the electrodes were immersed in BSA solution for 1 h, with the aim of having BSA molecules to block nonspecific active sites to the analyte. After each step the electrodes were washed to remove poorly or nonadsorbed molecules.

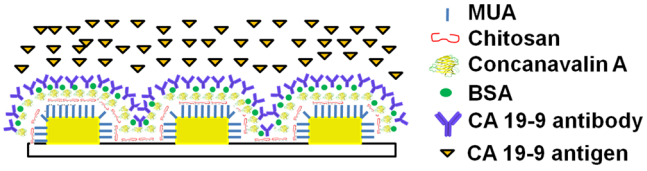

Figure 1. Film architecture that contains layers of MUA, chitosan, Con A modified with NHS groups, and CA19−9 antibody. Also shown are molecules of CA19−9 antigen to be detected.

Film Characterization. The adsorption of each layer in the architecture of Figure 1 was monitored with a Quartz Crystal Microbalance, model QCM200 (Stanford Research System, USA) for films deposited on quartz crystals coated with a gold disk electrode. Films were deposited on different types of substrate, depending on the experimental characterization technique. For polarization-modulated infrared reflection absorption spectroscopy (PM-IRRAS), the substrate used was gold. The PM-IRRAS spectra were obtained in a KSV spectrophotometer, model PMI 550 (KSV Instruments, Finland), with spectral resolution of 8 cm^{-1} and an incident angle of 81°. The contact angle and surface energy were determined using the sessile drop technique in a goniometer model CAM200 (KSV Instruments, Finland), using deionized water, ethylene glycol and diiodomethane as probe liquids for films deposited on the interdigitated gold electrodes. The data for these probe liquids were used in the Owens−Wendt−Rabel−Kaelble model[30] to calculate the different components of surface energy, using eqs 1 and 2

$$\left(\frac{(1+\cos(\theta)\gamma_L)}{2\sqrt{\gamma_L^d}}\right) = \sqrt{\gamma_S^p}\left[\frac{\sqrt{\gamma_L^p}}{\sqrt{\gamma_L^d}}\right] + \sqrt{\gamma_S^d} \quad (1)$$

$$\gamma_S = \gamma_S^d + \gamma_S^p \quad (2)$$

where γ_S is the surface energy, γ_L is the liquid surface tension, θ is the angle between solid−liquid surface, γ_L^d,γ_S^d,γ_L^p, and γ_S^p are polar (p) and dispersive components (d) of the solid and liquid surface tension.

The morphology of films deposited on the interdigitated gold electrodes was investigated with atomic force microscopy (AFM) in a Bruker Dimension FastScan (Bruker Corp., USA) microscope in the Tapping mode with scan rate of 0.6 Hz. Fluorescence spectroscopy measurements were carried out with a spectrophotometer Shimadzu (Shimadzu Corp., Japan) model RF 530 IPC.

Detection. Impedance spectroscopy measurements were performed with a Solartron model 1260 A (Solartron Analytical, USA), in the range between 1×10^2 and 1×10^6 Hz, with biosensors whose architecture is shown in Figure 1. Interdigitated electrodes modified as described in the Electrode Modification were used to detect CA19−9 human antigen (Aviva System Biology, USA). A solution of CA19−9 at different concentrations (4, 8, 12, 20, 40, 60, 80, and 100 U/mL) was dropped on the sensing unit and allowed for adsorption during 10 min. The film was then washed and immersed into a PBS buffer, so that only changes in the capacitance induced by specific adsorption would be measured. The data collected were used to obtain a calibration curve, with which the CA19−9 concentration could be determined in fetal bovine serum (FBS) (Sigma-Aldrich, USA) and cell lines HT-29 (ATCC, HTB-38) and SW-620 (ATCC, CCL-227). Both cell lines were maintained in Dulbecco's modified eagle's medium (DMEM) or RPMI 1640, containing 10% fetal bovine serum (FBS), 2 mM glutamine, 1% penicillin/streptomycin, in a humidified CO_2 incubator at 37 °C. Confluent cell lines were washed with phosphate-buffered saline (PBS) and cultured in OptiMEM media, without serum supplementation. After 48 h of incubation, the supernatant was filtered through a 0.22 μm filter and stored at −80 °C until analysis. The concentration of CA19−9 was obtained through an electrochemiluminescence immunoassay (ECLIA), performed in a commercially available assay (Roche Diagnostics, USA; Catalog number 11776193122) in Cobas e 601 (Roche Diagnostics, USA). The calibration curve was calculated with Elecsys CA 19−9 CalSet (Roche Diagnostics, USA).

DOI: 10.1021/acsami.5b08666
ACS Appl. Mater. Interfaces 2015, 7, 25930−25937

Data Treatment with Information Visualization Methods. The capacitance values, obtained from impedance measurements, were analyzed using the software suite referred as PEx-Sensors,[26] which implements multidimensional projection and information visualization techniques, such as Interactive Document Mapping (IDMAP) and Parallel Coordinates.[26−28] The first technique considers Euclidean distances between the signals of different samples $X = \{x_1, x_2, ..., x_n\}$, with $\delta(x_i,x_j)$ being dissimilarity functions between two samples (i and j). From this, the data in X are projected into a lower-dimension space, where $Y = \{y_1, y_2, ..., y_n\}$ gives the position of visual elements (mappings of X) and $d(y_i - y_j)$ is distance functions of two any elements of mappings of X. These projections follow a injective function f: $X \rightarrow Y$, which minimize the term $|\delta(x_i,x_j) - d(y_i - y_j)|\forall x_i,x_j) \in X$, and is given by eq 3, where δ_{max} and δ_{min} are the maximum and minimum distances between data instances.

$$S_{IDMAP} = \frac{\delta(x_i, x_j) - \delta_{min}}{\delta_{max} - \delta_{min}} - d(y_i, y_j) \quad (3)$$

For this, we use the parallel coordinates techniques,[31,32] which map the instances data set as equally spaced parallel axes that are scaled to depict the range of measured values. Capacitance values are determined by the intersection of the frequency axis in the points to be measured. Through this visual representation, we observe the data distribution, in addition to their correlations.[26,27]

RESULTS AND DISCUSSION

Confirming the Film Architecture for the Sensing Units. One of the main advantages of using nanostructured films to produce immnunosensors is the versatility in the choice of materials to be combined in a synergistic fashion. Unfortunately, there is no general rule to dictate which and how the materials are to be combined, and therefore a systematic study needs to be conducted for optimizing the film architecture. In this work, we used four experimental methods to determine the optimized conditions for film fabrication, and exploiting the architecture shown in Figure 1. Accordingly, we used a quartz crystal microbalance to measure the mass adsorbed in each layer, photoluminescence spectroscopy to confirm adsorption of Con A, contact angle measurements to determine surface energy and PM-IRRAS to confirm the overall film architecture. Figure S1 shows the mass determined via QCM for the different layers. Chitosan adsorption was maximum for solution concentrations at 1−2 mg/mL, because saturation tends to occur for very high concentrations. In fact, a larger amount of chitosan was adsorbed for 1 mg/mL than for 2 mg/mL, probably because some desorption takes place at higher concentrations. For a fixed Con A concentration, we found the expected result of higher amount of Con A for the 1 and 2 mg/mL chitosan concentrations. The stronger Con A adsorption for the layer obtained with 1 mg/mL chitosan was confirmed in photoluminescent experiments, in which the Con A solution had its spectrum measured before and after the adsorption procedure. Figure S2 brings this piece of data. We shall show that under these optimized conditions, the sensitivity is higher because of the larger amount of adsorbed anti-CA19−9 antibodies.

The stronger adsorption of chitosan and Con A for the 1 mg/mL chitosan concentration leads to film surfaces with higher surface energy (more hydrophilic). This has been determined by measuring the contact angle of the films after each deposition step with three probe liquids, and the data are shown inFigure S3. The surface is considerably more hydrophilic when a chitosan/Con A bilayer is deposited with the 1 mg/mL solution. This leads to a higher surface energy, as obtained with the Owens−Wendt−Rabel−Kaelble model[30] mentioned in the Film Characterization section and shown in Figure S4. A higher surface energy is advantageous for adsorption of biomolecules, which has a positive effect on the detection performance of the electrodes, as will be shown later.

The characterization above allowed us to select film architectures with higher probability of adequate sensing performance, but the actual architecture could not be inferred precisely. We have therefore monitored the deposition of each layer with PM-IRRAS, which makes it possible to determine the characteristic bands of functional groups. The PM-IRRAS spectra for the 4 chitosan:Con A conditions always confirmed the adsorption of the planned layers, and the spectra for the two most efficient conditions are shown in Figure 2.

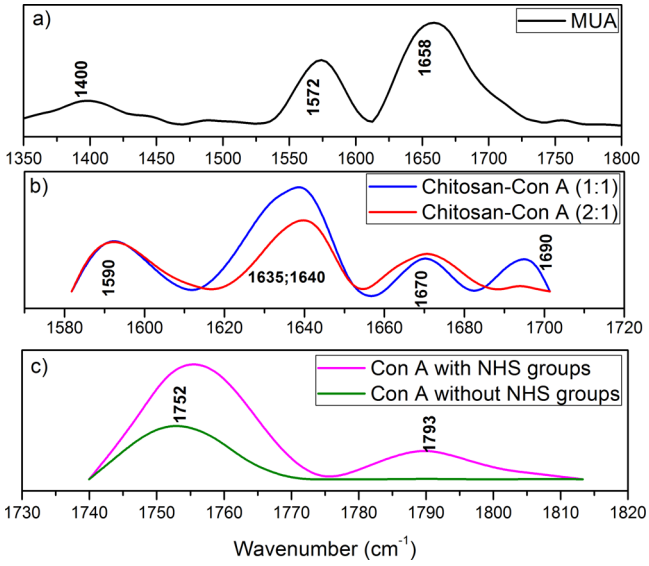

Figure 2. PM-IRRAS spectra of layers (a) Au/Mua, (b) Au/Mua/chitosan(n)/Con A(n), (c) functionalized with native Con A and Con A modified with NHS groups.

Functionalization with 11-MUA is confirmed in Figure 2a by the bands at 1568 cm^{-1} (C═O deformation), 1572 cm^{-1} (COO^- symmetric stretch), 1487 and 1400 cm^{-1} (CH_2 bending).[33−35] With adsorption of a layer of chitosan and another of Con A, Figure 2b shows bands assigned to the axial deformation of amide II at 1593 cm^{-1} from chitosan, to β-sheets and antiparallel β-sheets of Con A at 1635/1640 and 1693 cm^{-1}, respectively,[33,36] and to β-turn structures at 1670 cm^{-1}[34]. Consistent with the QCM data, a larger amount of material is adsorbed for the 1 mg/mL chitosan concentration, which is inferred by estimating the integrated areas for the band at 1630/1640, 1670, and 1690 cm^{-1}. The success of the procedure to activate the carboxylate groups from Con A with NHS-EDC is depicted in Figure 2c, featuring the symmetrical stretching band of NHS carbonyl at 1790 cm^{-1},[33] thus indicating that the imine groups have coupled to Con A.

Detecting CA19−9 with Impedance Spectroscopy. The two film architectures built with 2 and 1 mg/mL chitosan solutions, which we shall hereon refer to as Sensors A and B, respectively, were employed in three types of detection experiments. In the first, we used samples with PBS buffer containing different concentrations of the commercial CA19−9 antigen biomarker (Aviva System Biology, USA); in the second type, measurements were made with samples obtained from

DOI: 10.1021/acsami.5b08666
ACS Appl. Mater. Interfaces 2015, 7, 25930−25937

two cell lines, one of which contained CA19−9; in the third type, measurements were performed with commercial CA19−9 immersed in fetal bovine serum (FBS). Figure 3 shows the

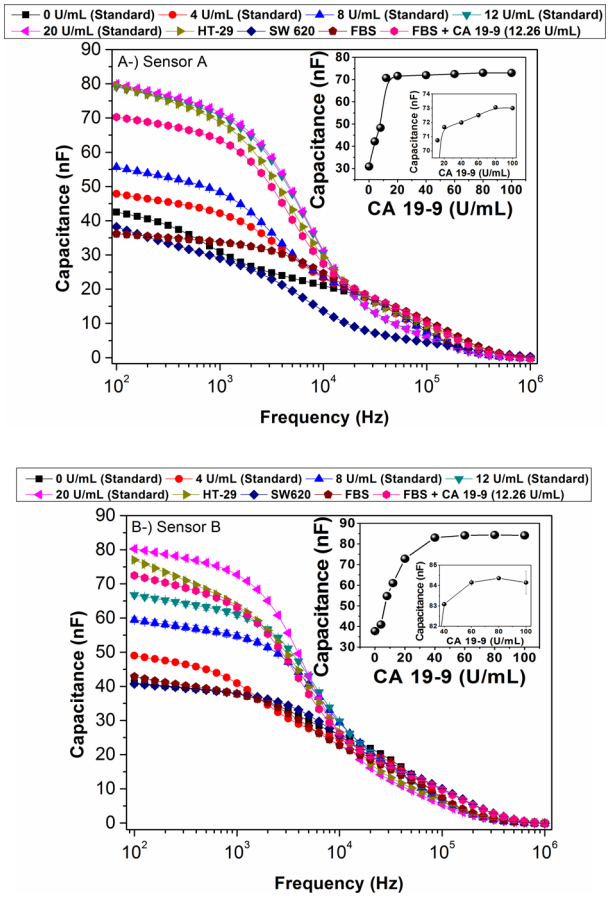

Figure 3. Capacitance vs. frequency spectra for (a) Sensor A and (b) Sensor B, immersed in PBS solutions with different CA19−9 concentrations. The insets show the capacitance (nF) versus CA19−9 concentration at 1 kHz, also including data for higher concentrations whose spectra are shown in Figure S5. Capacitance values increase until saturation, which is typical of immunosensors with antigen−antibody interactions. The capacitance was calculated from the complex impedance equation.[39]

frequency dependence for the capacitance in Sensors A and B, exposed to varying concentrations of commercial CA19−9, two samples obtained with the cell lines HT-29 and SW620 and CA19−9 (12.26 U/mL) immersed in FBS. In the low-frequency region there is considerable distinction among the curves, which indicates that the electrical response of the sensing units is affected by interaction with CA19−9. The mechanisms governing such an interaction should be associated with changes induced by CA19−9 on the double-layer existing at the interface between film and the buffer solution and on the film itself. For it is known from the literature[37,38] that the electrical response is dominated by changes in the double-layer at frequencies around and below 100 Hz, whereas film properties dominate the response in the 1 kHz region. Exposure to the CA19−9 containing samples had little effect on the capacitance at very high frequencies, which depends mostly on changes in the geometric capacitance.[37]

The insets in Figure 3 indicate saturation in the capacitance change as the CA19−9 concentration increases, which is typical of immunosensors based on antigen−antibody interactions because the number of available sites for adsorption tends to zero. Taking the initial part of the curves, which may be approximated by a straight line, we could determine the limit of detection for each sensor, using the IUPAC method. These limits of detection were found to be 0.91 U/mL and 0.69 U/mL for Sensors A and B, respectively, which are lower than the commercial systems Architect i2000 (Abbott Laboratories, USA), AxSYM (Abbott Laboratories, USA), and KRYPTOR (Brahms Aktiengesellschaft, Germany) (2; 2; 1.2 U/mL, respectively), being comparable to that of Elecsys (Roche Diagnostics GmbH, Germany) (0.6 U/mL).[40] Furthermore, the various concentrations can be distinguished up to 76.8 and 51.8 U/mL for Sensors A and B, respectively, therefore being above the cutoff limit (37 U/mL) for patients with pancreas cancer.[41,42] This feature of the immunosensors is crucial for their possible use in prognostics and early diagnostics. Also significant is that the curves for HT29 and CA 19−9 immersed in FBS solution were considerably distinct from the PBS buffer, as it should be since they contained CA19−9. In fact, in subsidiary experiments, the CA19−9 concentration in HT29 was found to be 12.26 U/mL, which compares well with the values extracted from the calibration curves in the insets, namely 11.7 and 13.7 U/mL for Sensors A and B, respectively. In contrast, the cell line SW620 gave curves very similar to PBS, being negative for CA19−9 antigen, as it should be.[43] For CA19−9 immersed in FBS at 12.26 U/mL, the concentration

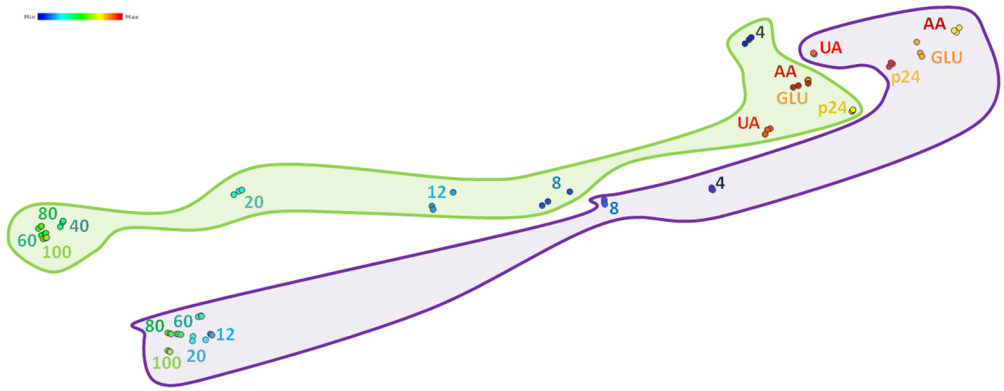

Figure 4. IDMAP plot for the data of change in capacitance × frequency curves for standard samples containing distinct concentrations of CA19−9 as specified in the figure, and nonspecific analytes (p24 antigen, UA, AA, GLU) for Sensor A (purple) and Sensor B (green).

DOI: 10.1021/acsami.5b08666
ACS Appl. Mater. Interfaces 2015, 7, 25930−25937

inferred from the capacitance data was 11.5 U/mL and 13.2 U/mL for sensor A and sensor B, respectively.

As mentioned in the Introduction, using impedance spectroscopy for immunosensing is advantageous in several ways, particularly regarding the generality of the sensing platform and potential low cost. However, the main possible drawback is the lack of specificity in the electrical response, because any change in the sample under analysis and in the film of the sensing unit itself may lead to alterations in the electrical signal. Therefore, it is of paramount importance to test the performance of the immunosensors in relation to false positives. We have made a thorough, systematic study to ensure that our immunosensors are robust and selective for detecting CA19−9. First, we exposed Sensors A and B to a variety of analytes and nonspecific antigens. Figure 4 shows the impedance data projected in an IDMAP plot for false positive tests for both sensors. A clear separation is seen of the CA19−9 standard (commercial) samples from the analytes ascorbic acid (AA), uric acid (UA), glucose (GLU), and the antigen p24.

In a second type of experiment, we compared the response of Sensors A and B with that of sensing units which did not contain the anti-CA19−9 antibodies immobilized on the film surface. The results are shown in Figure 5, which demonstrate a negligible change in capacitance for the sensing units with no antibody, in comparison with the large changes for Sensors A and B. Therefore, it is once more confirmed that a significant change in the electrical response only takes place if there is adsorption of antigens on the film surface.

Comparison between Sensors A and B. Optimizing the performance of immunosensors may be crucial in applications where high sensitivity and/or selectivity is required, and in cases where there are several components in the sensing unit. Here we employ a methodology that allows us to compare sensor performance quantitatively, which could also be used to further optimize performance if needed. We plotted the capacitance data of Figure 3 and Figure S5 using the parallel coordinates technique in Figure 6. A visual inspection indicates that it is easier to distinguish the curves at low to intermediate frequencies, as commented upon while discussing Figure 3. The ability to distinguish among the many curves can be estimated quantitatively using the silhouette coefficient, calculated from eq 4.

$$S = \frac{1}{n}\sum_{i=1}^{n}\frac{b_i - a_i}{\max(a_i, b_i)} \tag{4}$$

The coefficient S varies between −1 to 1, and its value is represented by the boxes on the top of the plot in Figure 6. Blue boxes indicate that the curves at the particular frequency are distinct from each other, with S values near 1, whereas the white boxes ($S \sim 0$) indicate that the data do not assist in distinguishing the samples and the red boxes ($S \sim -1$) mean that using data at these frequencies may actually be deleterious for the distinction. The average silhouette coefficients is 0.861 for Sensor A and 0.853 for Sensor B, which means that Sensor A has a slightly higher performance.

The excellent performance of Sensors A and B may also be checked visually in the IDMAP plots of Figure 7. There is clear distinction between the samples with different concentrations of CA19−9, and the cell lines HT29 and SW620 give positive and negative result, respectively, for the presence of CA19−9.

On the Mechanisms Behind Detection. The immunosensor presented here was conceived to detect the antigen

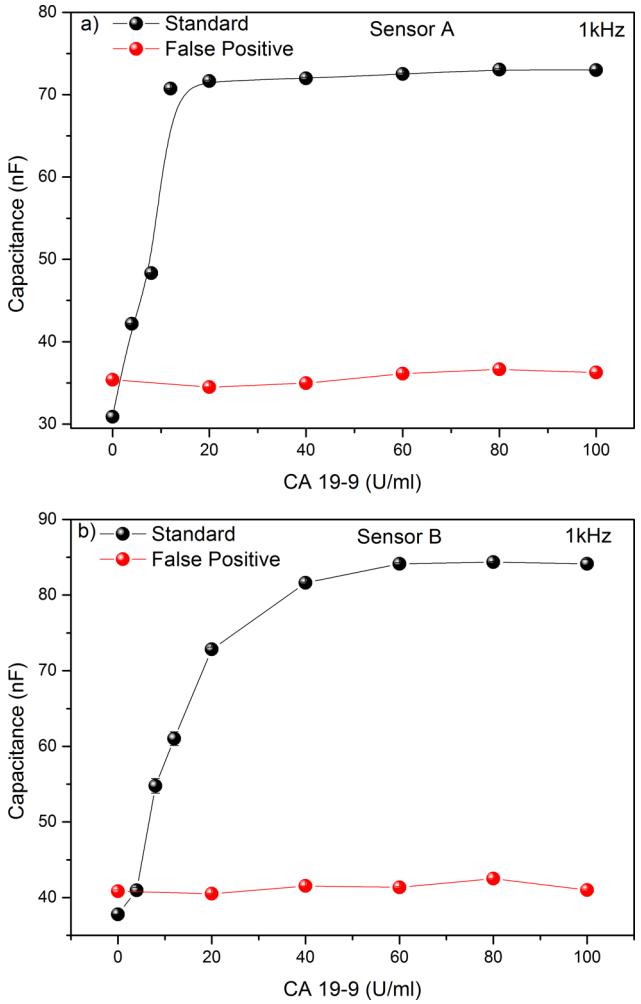

Figure 5. Capacitance at 1 CA19−9 concentration for (a) Sensors A and (b) B in black lines, compared to the lack of change in capacitance when the CA19−9 concentration is varied for a sensing unit that did not contain anti-CA19−9 antibodies (in red lines). The latter are terms as possible false positives, which did not occur in our measurements.

CA19−9 based on the molecular recognition capability toward its corresponding antibody. The detection experiments were successful, but we have not proven yet that sensing was governed by the specific adsorption. This we can prove using PM-IRRAS measurements. We used as reference the spectrum of the film MUA/Chitosan/Con A-NHS, in order to investigate the interaction between the anti-CA19−9 antibodies and the antigen CA19−9. The other regions of the spectra for the film were not affected by the adsorption of the antibody and then of the antigen. Figure 8 shows characteristic amide I and amide II bands which are present in both antibody and antigen. The amide I band appears between 1600 and 1700 cm^{-1}, and is mainly represented by 80% of the potential energy associated with the carbonyl stretch (C═O), 10% of C−N stretch, and 10% related to the N−H bond vibration.[33,44] The amide II band is observed between 1500 and 1600 cm^{-1}, for which 60% of the potential energy are related to N−H bonds, whereas the remaining 40% are assigned to the C−N bond stretch of amide groups.[33,44] The intensity (and area) of these bands increase with the CA19−9 concentration until getting close to saturation, as expected. Consistent with the results from impedance spectroscopy, Sensor B is more sensitive than

DOI: 10.1021/acsami.5b08666
ACS Appl. Mater. Interfaces 2015, 7, 25930−25937

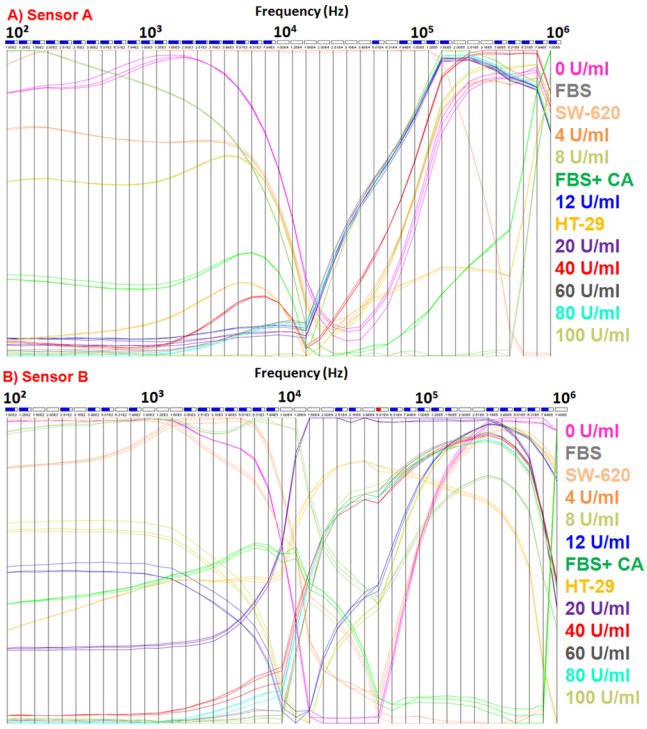

Figure 6. Parallel coordinates plot obtained from capacitance x frequency curves measured with Sensors A and B for different CA19−9 antigen concentrations. The abscissa corresponds to frequency, whereas the ordinate brings normalized values of capacitance.

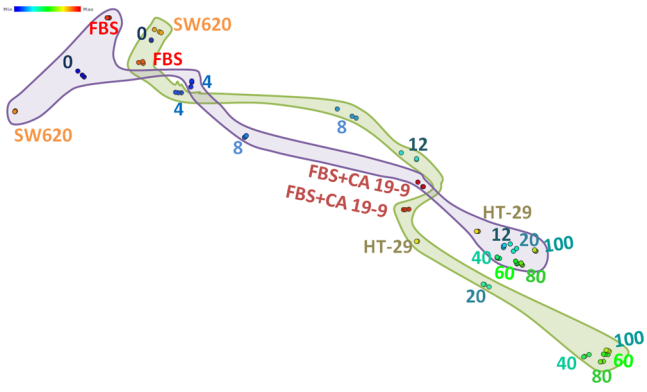

Figure 7. IDMAP plot obtained from the capacitance × frequency curves for CA19−9 commercial samples in PBS, HT-29, and SW620 cell lines and CA19−9 commercial samples in FBS solution for Sensor A (purple) and Sensor B (green).

Sensor A. In this analysis, we assumed that the orientation of the amide groups will not vary when the CA19−9 is altered; otherwise we could not relate the intensity of the PM-IRRAS band with the concentration of CA19−9 detected.

The adsorption of antigen CA19−9 molecules onto immobilized antibodies of the film was further confirmed with AFM images in Figure S6, which again corroborated the stronger adsorption of chitosan/Con A and hence antibodies anti-CA19−9.

CONCLUSIONS

Nanostructured films have been used here to produce immunosensors that were capable of detecting small concentrations of CA19−9, and identify cell lines that contained this

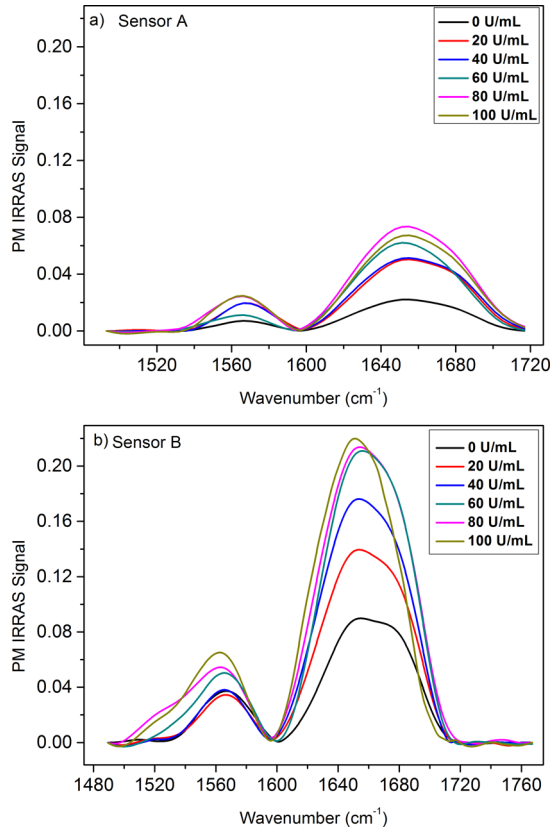

Figure 8. PM-IRRAS spectra for the films used to build Sensors A and B. The baseline was taken as the spectrum for the film architecture gold/MUA/chitosan/Con A-NHS, onto which a layer of antibodies was immobilized, then followed by adsorption of the antigen CA19−9 with different concentrations.

biomarker. The choice of film components proved to be suitable, as the antibodies were adequately immobilized so as to recognize the CA19−9 antigen specifically. In detection with impedance spectroscopy, for example, no false positives were observed when the immunosensor was exposed to analytes and antigens other than CA19−9. Furthermore, the sensitivity with limit of detection of 0.69 U/mL is sufficient for applications in clinical analysis, being higher than most of the commercially available kits. The limit of detection in our sensors is not, however, as low as in an optimized electrochemical immunosensor using using a nano ferromagnetic oxide[5] and another with titania sol−gel on a graphite electrode that contained horseradish peroxidase (HRP)-labeled anti-CA19−9 antibodies.[4]

Two other important contributions in this study are related to the use of information visualization methods to compare the performance of sensors and biosensors, and the identification of the molecular-level mechanism responsible for the detection. With regard to comparing sensing units, we employed the parallel coordinates technique and calculated the silhouette coefficient that provides a quantitative measure of how useful a given signal is to distinguish among similar samples. The molecular-level mechanism was found to be associated with adsorption of antigens on their corresponding antibodies, and this has been proven by examining the amide bands in PM-IRRAS spectra.

DOI: 10.1021/acsami.5b08666
ACS Appl. Mater. Interfaces 2015, 7, 25930−25937

■ ASSOCIATED CONTENT

Supporting Information

The Supporting Information is available free of charge on the ACS Publications website at DOI: 10.1021/acsami.5b08666.

Complementary characterization of immunosensor architectures (PDF)

■ AUTHOR INFORMATION

Corresponding Author

*E-mail: andreycoatrini@gmail.com.

Notes

The authors declare no competing financial interest.

■ ACKNOWLEDGMENTS

The authors thank FAPESP (Grant 2013/14262-7), CNPq, CAPES, and nBioNet network for the financial support and Barretos Cancer Hospital. Acknowledgments are also given to Angelo L. Gobbi and Maria H. O. Piazzetta for use of the microfabrication laboratory (LMF/LNNano-LNLS).

■ REFERENCES

(1) Kearney, A. J.; Murray, M. Breast Cancer Screening Recommendations: is Mammography the Only Answer? *J. Midwifery Womens Health* **2009**, *54*, 393−400.

(2) Gullick, W. J. Update on HER-2 as a Target for Cancer Therapy: Alternative Strategies for Targeting the Epidermal Growth Factor System in Cancer. *Breast Cancer Res.* **2001**, *3*, 390−394.

(3) Li, L.; Zhang, L.; Yu, J.; Ge, S.; Song, X. All-Graphene Composite Materials for Signal Amplification Toward Ultrasensitive Electrochemical Immunosensing of Tumor Marker. *Biosens. Bioelectron.* **2015**, *71*, 108−114.

(4) Du, D.; Yan, F.; Liu, S.; Ju, H. Immunological Assay for Carbohydrate Antigen 19−9 Using an Electrochemical Immunosensor and Antigen Immobilization in Titania Sol−Gel Matrix. *J. Immunol. Methods* **2003**, *283*, 67−75.

(5) Zhang, Q.; Chen, X.; Tang, Y.; Ge, L.; Guo, B.; Yao, C. Amperometric Carbohydrate Antigen 19−9 Immunosensor Based on Three Dimensional Ordered Macroporous Magnetic Au Film Coupling Direct Electrochemistry of Horseradish Peroxidase. *Anal. Chim. Acta* **2014**, *815*, 42−50.

(6) Oliveira, O. N., Jr; Iost, R. M.; Siqueira, J. R.; Crespilho, F. N.; Caseli, L. Nanomaterials for Diagnosis: Challenges and Applications in Smart Devices Based on Molecular Recognition. *ACS Appl. Mater. Interfaces* **2014**, *6*, 14745−14766.

(7) Cennamo, N.; Pesavento, M.; Lunelli, L.; Vanzetti, L.; Pederzolli, C.; Zeni, L.; Pasquardini, L. An Easy Way to Realize SPR Aptasensor: A Multimode Plastic Optical Fiber Platform for Cancer Biomarkers Detection. *Talanta* **2015**, *140*, 88−95.

(8) Zhang, Y.; Yang, D.; Weng, L.; Wang, L. Early Lung Cancer Diagnosis by Biosensors. *Int. J. Mol. Sci.* **2013**, *14*, 15479−15509.

(9) Ravalli, A.; Marrazza, G. Gold and Magnetic Nanoparticles-Based Electrochemical Biosensors for Cancer Biomarker Determination. *J. Nanosci. Nanotechnol.* **2015**, *15*, 3307−3319.

(10) Wink, T.; Van Zuilen, S. J.; Bult, A.; Van Bennekom, W. P. Self-Assembled Monolayers for Biosensors. *Analyst* **1997**, *122*, 43−50.

(11) Chen, H.; Guo, X. Unique Role of Self-Assembled Monolayers in Carbon Nanomaterial-Based Field-Effect Transistors. *Small* **2013**, *9*, 1144−1159.

(12) Ariga, K.; Yamauchi, Y.; Rydzek, G.; Ji, Q.; Yonamine, Y.; Wu, K. C. W.; Hill, J. P. Layer-by-layer Nanoarchitectonics: Invention, Innovation, and Evolution. *Chem. Lett.* **2014**, *43*, 36−68.

(13) Rydzek, G.; Ji, Q.; Li, M.; Schaaf, P.; Hill, J. P.; Boulmedais, F.; Ariga, K. Electrochemical Nanoarchitectonics and Layer-by-Layer Assembly: From Basics to Future. *Nano Today* **2015**, *10*, 138−167.

(14) Yue, T.; Partyka, K.; Maupin, K. A.; Hurley, M.; Andrews, P.; Kaul, K.; Moser, A. J.; Zeh, H.; Brand, R. E.; Haab, B. B. Identification of Blood-Protein Carriers of the CA 19−9 Antigen and Characterization of Prevalence in Pancreatic Diseases. *Proteomics* **2011**, *11*, 3665−3674.

(15) Bauer, T. M.; El-Rayes, B. F.; Li, X.; Hammad, N.; Philip, P. A.; Shields, A. F.; Zalupski, M. M.; Bekaii-Saab, T. Carbohydrate Antigen 19−9 is a Prognostic and Predictive Biomarker in Patients with Advanced Pancreatic Cancer who Receive Gemcitabine-Containing Chemotherapy: A Pooled Analysis of 6 Prospective Trials. *Cancer* **2013**, *119*, 285−292.

(16) Xu, B.; Zheng, W. Y.; Jin, D. Y.; Ding, W.; Lou, W. H.; Ramsohok, L. Predictive Value of Serum Carbohydrate Antigen 19−9 in Malignant Intraductal Papillary Mucinous Neoplasms. *World J. Surg.* **2011**, *35*, 1103−1109.

(17) Tessler, D. A.; Catanzaro, A.; Velanovich, V.; Havstad, S.; Goel, S. Predictors of Cancer in Patients with Suspected Pancreatic Malignancy without a Tissue Diagnosis. *Am. J. Surg.* **2006**, *191*, 191−197.

(18) Hwang, D. W.; Jang, J. Y.; Lee, S. E.; Lim, C. S.; Lee, K. U.; Kim, S. W. Clinicopathologic Analysis of Surgically Proven Intraductal Papillary Mucinous Neoplasms of the Pancreas in SNUH: a 15-Year Experience at a Single Academic Institution. *Langenbecks Arch. Surg.* **2012**, *397*, 93−102.

(19) Duffy, M. J.; Sturgeon, C.; Lamerz, R.; Haglund, C.; Holubec, V. L.; Klapdor, R.; Nicolini, A.; Topolcan, O.; Heinemann, V. Tumor Markers in Pancreatic Cancer: a European Group on Tumor Markers (EGTM) Status Report. *Ann. Oncol.* **2010**, *21*, 441−447.

(20) Zhang, Y.; Yang, J.; Li, H.; Wu, Y.; Zhang, H.; Chen, W. Tumor Markers CA19−9, CA242 and CEA in the Diagnosis of Pancreatic Cancer: A Meta-Analysis. *Int. J. Clin. Exp. Med.* **2015**, *8*, 11683−11691.

(21) Jiang, X. T.; Tao, H. Q.; Zou, S. C. Detection of Serum Tumor Markers in the Diagnosis and Treatment of Patients with Pancreatic Cancer. *Hepatobiliary Pancreatic Dis. Int.* **2004**, *3*, 464−468.

(22) Ferrone, C. R.; Finkelstein, D. M.; Thayer, S. P.; Muzikansky, A.; Castillo, F.; Warshaw, A. L. Perioperative CA19−9 Levels Can Predict Stage and Survival in Patients with Resectable Pancreatic Adenocarcinoma. *J. Clin. Oncol.* **2006**, *24*, 2897−2902.

(23) Berger, A. C.; Garcia, M.; Hoffman, J. P.; Regine, W. F.; Abrams, R. A.; Safran, H.; Konski, A.; Benson, A. B., 3rd.; Macdonald, J.; Willett, C. G. Postresection CA 19−9 Predicts Overall Survival in Patients with Pancreatic Cancer Treated with Adjuvant Chemoradiation: a Prospective Validation by RTOG 9704. *J. Clin. Oncol.* **2008**, *26*, 5918−5922.

(24) Ballehaninna, U. K.; Chamberlain, R. S. Serum CA 19−9 as a Biomarker for Pancreatic Cancer-A Comprehensive Review. *Indian J. Surg. Oncol* **2011**, *2*, 88−100.

(25) Partyka, K.; Maupin, K. A.; Brand, R. E.; Haab, B. B. Diverse Monoclonal Antibodies Against the CA 19−9 Antigen Show Variation in Binding Specificity with Consequences for Clinical Interpretation. *Proteomics* **2012**, *12*, 2212−2220.

(26) Paulovich, F. V.; Moraes, M. L.; Maki, R. M.; Ferreira, M.; Oliveira, O. N., Jr; Oliveira, M. C. F. Information Visualization Techniques for Sensing and Biosensing. *Analyst* **2011**, *136*, 1344−1350.

(27) Moraes, M. L.; Petri, L.; Oliveira, V.; Olivati, C. A.; Oliveira, M. C. F.; Paulovich, F. V.; Oliveira, O. N., Jr; Ferreira, M. Detection of Glucose and Triglycerides Using Information Visualization Methods to Process Impedance Spectroscopy Data. *Sens. Actuators, B* **2012**, *166−167*, 231−238.

(28) Oliveira, O. N., Jr.; Neves, T. T. A. T.; Paulovich, F. V.; Oliveira, M. C. F. Where Chemical Sensors May Assist in Clinical Diagnosis Exploring "Big Data. *Chem. Lett.* **2014**, *43*, 1672−1679.

(29) Ron, H.; Matlis, S.; Rubinstein, I. Self-Assembled Monolayers on Oxidized Metals. 2. Gold Surface Oxidative Pretreatment, Monolayer Properties, and Depression Formation. *Langmuir* **1998**, *14*, 1116−1121.

(30) Owens, D. K.; Wendt, R. C. Estimation of the Surface Free Energy of Polymers. *J. Appl. Polym. Sci.* **1969**, *13*, 1741−1747.

(31) Heinrich, J.; Weiskopf, D. State of the Art of Parallel Coordinates. *STAR Proc. Eurograph* **2013**, 95−116.

DOI: 10.1021/acsami.5b08666
ACS Appl. Mater. Interfaces 2015, 7, 25930−25937

(32) Inselberg, A.; Dimsdale, B. Parallel Coordinates: A Tool for Visualizing Multi-Dimensional Geometry. *Proc. first IEEE Conf. Vis.* **1990**, 361−375.
(33) Colthup, N. B.; Daly, L. H.; Wiberley, S. E. Introduction to Infrared and Raman Spectroscopy; Academic Press: *New York*, 1964.
(34) Frey, B. L.; Corn, R. M. Covalent Attachment and Derivatization of Poly (L-Lysine) Monolayers on Gold Surfaces as Characterized by Polarization- Modulation FT-IR Spectroscopy. *Anal. Chem.* **1996**, *68*, 3187−3193.
(35) Barth, A. The Infrared Absorption of Amino Acid Side Chains. *Prog. Biophys. Mol. Biol.* **2000**, *74*, 141−173.
(36) Kong, J.; Yu, S. Fourier Transform Infrared Spectroscopic Analysis of Protein Secondary Structures. *Acta Biochim. Biophys. Sin.* **2007**, *39*, 549−559.
(37) Riul, A., Jr; Gallardo Soto, A. M.; Mello, S. V.; Bone, S.; Taylor, D. M.; Mattoso, L. H. C. An Electronic Tongue Using Polypyrrole and Polyaniline. *Synth. Met.* **2003**, *132*, 109−116.
(38) Taylor, D. M.; Macdonald, A. G. AC Admittance of the Metal/ Insulator/ Electrolyte Interface. *J. Phys. D: Appl. Phys.* **1987**, *20*, 1277−1283.
(39) Macdonald, J. R.; Barsoukov, E. *Impedance Spectroscopy: Theory, Experiment and Applications*; John Wiley & Sons: Hoboken, NJ, 2005.
(40) Passerini, R.; Riggio, D.; Salvatici, M.; Zorzino, L.; Radice, D.; Sandri, M. T. Interchangeability of Measurements of CA 19−9 in Serum with Four Frequently Used Assays: an Update. *Clin. Chem. Lab. Med.* **2007**, *45*, 100−104.
(41) Wang, Q.; Ji, Z.; Chen, Z.; Li, H.; Fan, H.; Fan, X.; Shi, B. B.; Fang, Y. Serum CA 19−9 as a Good Prognostic Biomarker in Patients with Bladder Cancer. *Int. J. Surg.* **2015**, *15*, 113−116.
(42) Chen, Y.-L.; Chen, C.-H.; Hu, R.-H.; Ho, M.-C.; Jeng, Y.-M. Elevated Preoperative Serum CA19−9 Levels in Patients with Hepatocellular Carcinoma Is Associated with Poor Prognosis after Resection. *Sci. World J.* **2013**, *2013*, 1−6.
(43) Frykholm, G.; Glimelius, B.; Richter, S.; Carlsson, J. Heterogeneity in Antigenic Expression and Radiosensitivity in Human Colon Carcinoma Cell Lines. *In Vitro Cell. Dev. Biol.* **1991**, *27*, 900−906.
(44) Wieckowski, A.; Korzeniewski, C.; Braunschweig, B. *Vibrational Spectroscopy at Electrified Interfaces*; Wiley: Hoboken, NJ, 2013.

DOI: 10.1021/acsami.5b08666
ACS Appl. Mater. Interfaces 2015, 7, 25930−25937